

Theoretical Modeling of J/ψ Yield Modifications in Proton (Deuteron) - Nucleus Collisions at High Energies

J. L. Nagle,¹ A. D. Frawley,² L. A. Linden Levy,³ and M. G. Wysocki¹

¹*University of Colorado at Boulder**

²*Florida State University†*

³*Lawrence Livermore National Laboratory‡*

(Dated: November 23, 2010)

Understanding the detailed production and hadronization mechanisms for heavy quarkonia and their modification in a nuclear environment presents one of the major challenges in QCD. Calculations including nuclear-modified parton distribution functions (nPDFs) and fitting of break-up cross sections (σ_{br}) as parameters have been successful at describing many features of J/ψ modifications in proton(deuteron)-nucleus collisions. In this paper, we extend these calculations to explore different geometric dependencies of the modifications and confront them with new experimental results from the PHENIX experiment. We find that no combination of nPDFs and σ_{br} , regardless of the nPDF parameter set and the assumed geometric dependence, can simultaneously describe the entire rapidity and centrality dependence of J/ψ modifications in d +Au collisions at $\sqrt{s_{NN}} = 200$ GeV. We also compare the data with coherence calculations and find them unable to describe the full rapidity and centrality dependence as well. We discuss how these calculations might be extended and further tested, in addition to discussing other physics mechanisms including initial-state parton energy loss.

I. INTRODUCTION

In proton(deuteron)-nucleus collisions at the Relativistic Heavy Ion Collider (RHIC), the nucleus is extremely Lorentz-contracted and thus the entire interaction and traversal of the nuclear target takes place on a time scale of order $0.1 \text{ fm}/c$. Thus, one expects coherence effects to play a significant role in the physics of particle production and hadronization. By studying heavy quarkonia states, one can postulate that the initial hard production of a $c\bar{c}$ pair can be factorized from the later traversal of that pair through the remainder of the nucleus. Many calculations have utilized this factorized approach in trying to understand the nuclear modification of J/ψ yields in proton(deuteron)-nucleus reactions (for example [1–4]). In this factorized framework, modification of initial $c\bar{c}$ pair production is accounted for via nuclear-modified parton distribution functions (nPDFs). After being produced, the disassociation of charm pairs and thus the additional reduction in the number of final-state J/ψ mesons is accounted for with a simple breakup cross section (σ_{br}). It is interesting to test this picture to see if the experimental data requires additional physics, including coherence effects and initial-state parton energy loss. This work presents an extension of this simple calculational framework and investigation of some of the key underlying assumptions.

II. CALCULATION DETAILS

In this section we describe the inputs required for the calculation of the nuclear modification factors (R_{pA} or R_{dA}) for various nuclear targets and centrality selections. First, the density of partons in the nucleus is modified relative to the parton distribution function (PDF) for nucleons. This nuclear-modified PDF reflects the modified parton density encountered by the projectile and results in a modified number of hard scatterings that create $c\bar{c}$ pairs from $g + g$, $q + g$, and $q + \bar{q}$ interactions. The state of the art calculation is the EPS09 nPDF parameter set with uncertainties represented by 31 different Hessian basis parameterizations as detailed in [5]. Because J/ψ production at high energies is dominated by interactions between gluons, we will consider $g + g$ interactions only in the calculations in this paper. Figure 1 shows the EPS09 gluon modification R_G at a $Q^2 = 9 \text{ GeV}^2$, the appropriate scale for production of the J/ψ . It can be seen that the nPDFs are not well constrained by experimental data, particularly the low- x gluon distributions which dominate the J/ψ production probability at forward rapidity at RHIC energies.

The second main effect is that after creating the $c\bar{c}$ pair in the initial state (often referred to as the J/ψ precursor, since the hadronic state is expected to take of order $0.3 \text{ fm}/c$ to form), the pair may break up or be de-correlated while traversing the remaining portion of the nucleus. This second effect is often included by assuming a fixed cross section σ_{br} for the breakup of the pair. We note that this effect is also often termed absorption, though this nomenclature can be misleading since the charm pair still exists, but is no longer able to form a final-state J/ψ meson. Currently there is no fundamental description of the hadronization process for the J/ψ meson that agrees with all the available experimental data [6, 7]. The lack

* jamie.nagle@colorado.edu

† aefrawley@fsu.edu

‡ lindenle@llnl.gov

of such a theory for the dynamics of hadronization means one has no *ab initio* calculations of this precursor-nucleon cross section and its dependence on the relative velocity between the pair and the target nucleons. In most works, the value of σ_{br} is assumed to be independent of the J/ψ rapidity for a given $\sqrt{s_{NN}}$, and is determined from fits to the experimental data [8].

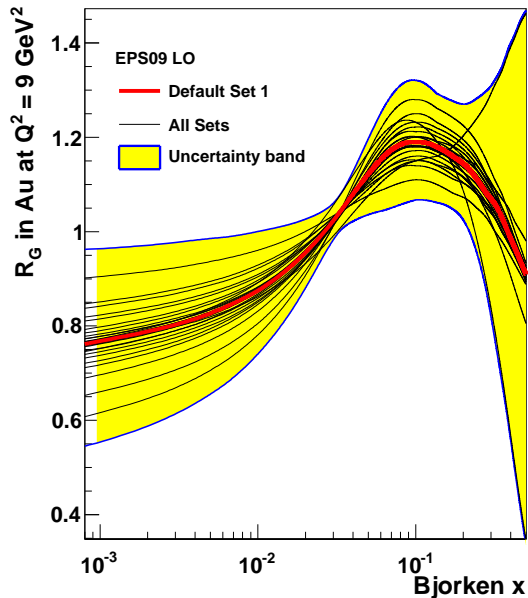


FIG. 1. The gluon nuclear modification R_G for the Au nucleus at the scale $Q^2 = 9 \text{ GeV}^2$ is shown for the EPS09 central value (labeled set 1) and for all 30 error sets. The yellow shaded area is the overall uncertainty band calculated from the error sets, representing a 90% CL uncertainty. The parameter sets from top to bottom at the lowest x values are 16, 10, 7, 8, 13, 31, 26, 18, 15, 4, 3, 21, 23, 25, 28, 1, 29, 2, 24, 20, 22, 14, 5, 19, 27, 30, 6, 12, 9, 11, 17.

We employ a Monte Carlo Glauber model [9] where the nucleons are randomly given spatial distributions within the deuteron based on the Hulthen wave function and for the gold nucleus based on a Woods-Saxon distribution with parameters $R=6.38 \text{ fm}$ and $a=0.54 \text{ fm}$ [2]. Individual $d+\text{Au}$ collisions at $\sqrt{s_{NN}} = 200 \text{ GeV}$ are simulated by randomly selecting an event impact parameter (b) and determining if any pair of nucleons collide using an inelastic cross section of $\sigma = 42 \text{ mb}$. One example event is shown in Figure 2, where the open circles are the positions of the gold nucleus nucleons in the transverse plane, the red filled circles are the positions of the two nucleons from the deuteron, and the green filled circles are the gold nucleus nucleons which suffered a binary collision. Each binary collision between a red circle (deuteron nucleon) and a green circle (gold nucleon) has a probability to produce a $c\bar{c}$ pair. This probability is modified from proton-proton collisions according to the afore-mentioned nPDFs.

The EPS09 nPDF parameterization, as well as other nPDF parameterizations, are predominantly determined from deep inelastic scattering experiments and minimum bias $p + A$ reactions producing Drell-Yan pairs [5]. In such experiments there is no measure of the impact parameter or transverse distance within the nucleus for the interaction and therefore the geometric dependence of the nPDF modification is not constrained. One expects a significant geometric dependence in the nPDF modification, with a stronger modification near the center of the nucleus where the density of nucleons is the largest. In a simple picture, the partons inside the nucleons at low- x have wave functions that are longer in the longitudinal direction than the Lorentz contracted nucleus. Thus the nPDF modification depends on the density of overlapping nucleons as shown in the transverse plane in Figure 2. However, there is no such Lorentz contraction in the transverse direction, and the parton wavefunction extent in this plane is of order 1 fm. Therefore, the largest nuclear effect would be expected where the density, and thus the longitudinal overlap is largest, near the center of the nucleus and should decrease as one moves out toward the periphery.

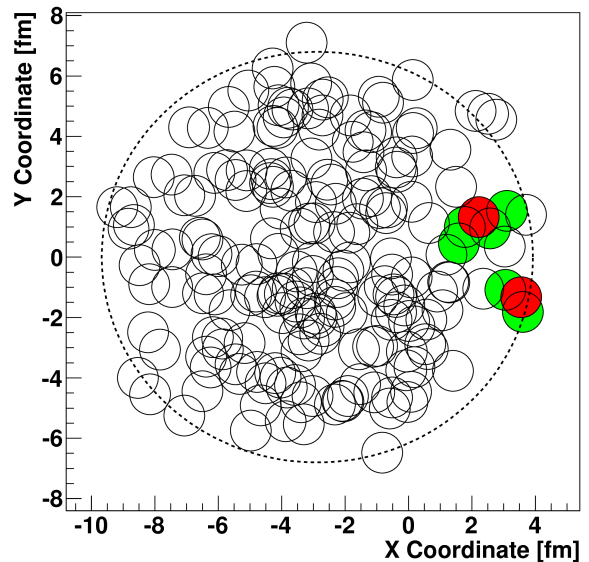


FIG. 2. Monte Carlo Glauber event display in the transverse (x - y) plane. Open black circles are the positions of the gold nucleus nucleons. Red filled circles are the positions of the two nucleons from the deuteron. Green filled circles are the positions of the gold nucleus nucleons which suffer at least one binary collision. The dashed black circle represents gold nucleus extent from the Woods-Saxon parameterization.

In [10], the nPDF modification is postulated to be linearly proportional to the density-weighted longitudinal thickness of the nucleus at the transverse position of the binary collision, as written below:

$$M(r_T) = 1.0 - a\Lambda(r_T) \quad (1)$$

where $\Lambda(r_T) = \frac{1}{\rho_0} \int dz \rho(z, r_T)$ is the density-weighted

longitudinal thickness and ρ_0 is the density at the center of the nucleus. In Figure 2, each green circle is a transverse distance r_T from the center of the gold nucleus, and one can then determine the average local thickness $\Lambda(r_T)$ based on the Woods-Saxon parameterization.

As shown in Figure 2, there are significant fluctuations in the thickness $\Lambda(r_T)$ due to the randomly selected spatial locations of the nucleons in the gold nucleus at the time of the collision. In fact, the inclusion of such fluctuations has proven to be crucial in modeling the initial conditions in heavy ion reactions (see for example [11–15]). In order to incorporate these fluctuations, we calculate the number of target nucleons around the struck nucleon (green circle) within a transverse radius $R_{tube} = 2 \times R_{nucleon}$, where $R_{nucleon}$ is taken to be the charge radius of the proton, 0.87 fm [16]. The average number of nucleons within this cylinder N_{tube} is $\pi R_{tube}^2 \rho_0$ times $\Lambda(r_T)$, and this proportionality constant can be absorbed into the parameter a in Eqn. 1. The exact choice of R_{tube} is somewhat arbitrary, but reasonable changes in the value do not significantly change the results shown in this paper.

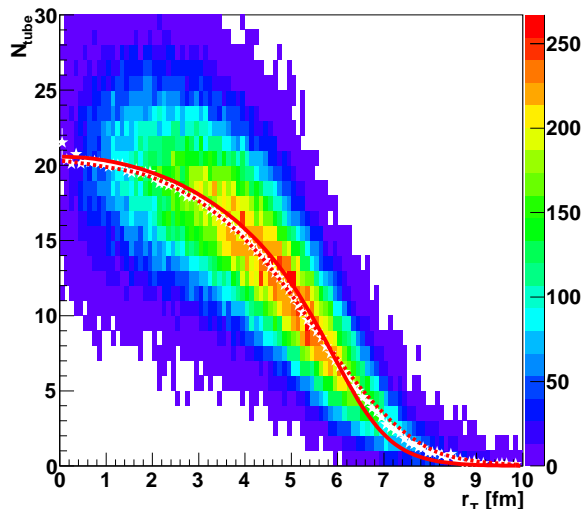


FIG. 3. Shown is the Monte Carlo Glauber result for the N_{tube} distribution as a function of r_T . The mean values of N_{tube} as a function of r_T are shown as white points. The analytic calculation of the average value of $\Lambda(r_T)$ from the Woods-Saxon parameterization, rescaled to the N_{tube} value, is shown as the solid red curve. Smearing the analytic calculation around r_T by the tube radius R_{tube} is shown as the red dashed curve.

In Figure 3 the resulting distribution of N_{tube} values as a function of r_T is shown. For collisions in the middle of the nucleus ($r_T \approx 0$) $\langle N_{tube} \rangle \approx 20$ and the RMS ≈ 5 . Using the analytic calculation of the average $\Lambda(r_T)$ from the Woods-Saxon parameterization times $\pi R_{tube}^2 \rho_0$ yields the solid red curve. The difference between the two is because the $N_{tube}(r_T)$ calculation includes the density averaged over the tube radius R_{tube} . If we smear the

analytic calculation around r_T by the tube radius R_{tube} , we obtain the red dashed curve, which now shows much better agreement.

In our calculations, we take these fluctuations into account by utilizing N_{tube} instead of the average $\Lambda(r_T)$, as shown in the equation below:

$$M(r_T) = 1.0 - aN_{tube}(r_T) \quad (2)$$

There is a direct relationship between the parameter a and the $\langle M \rangle$, the modification averaged over all nuclear geometries, which is equivalent to $R_{dAu}(0-100\%)$. This relationship is determined by averaging M over the r_T distribution for unbiased collisions as determined from the Monte Carlo Glauber (shown in Figure 3 of the PHENIX publication [17]). The results are shown as the red curve in Figure 4. We also consider two other geometric dependencies for the nPDF, referred to as exponential and quadratic.

$$M(r_T) = \text{Exp}(-aN_{tube}(r_T)) \quad (3)$$

$$M(r_T) = 1.0 - a[N_{tube}(r_T)]^2 \quad (4)$$

The same procedure is applied, and the dependence of the parameter a is also shown in Figure 4 as the black (blue) curve for the exponential (quadratic) case.

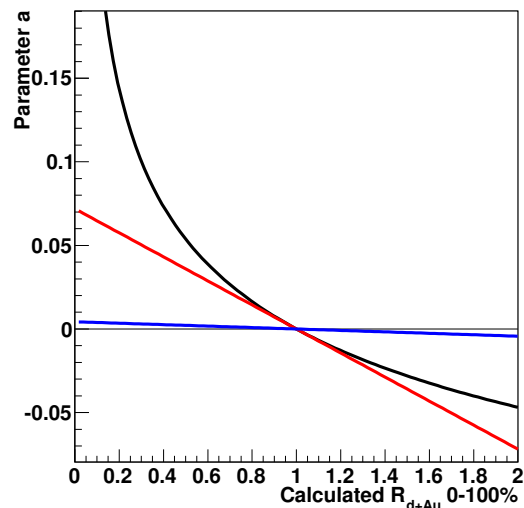


FIG. 4. Shown is the parameter a as a function of the $R_{dAu}(0-100\%)$ modification that is obtained. The red, black, and blue curves correspond to the linear, exponential, and quadratic geometric dependence cases respectively.

We examine the modification $M(r_T)$ for each of these cases. Shown in Figure 5 (left panel) is $M(r_T)$ for the exponential case. The four solid black curves correspond to geometry averaged modifications of $\langle M \rangle = 0.8, 0.6, 0.4, 0.2$ for the top to bottom curves. The dot-dashed black line is the shape of the mean of the N_{tube} distribution versus r_T , normalized to one at $r_T = 0$ for reference. The

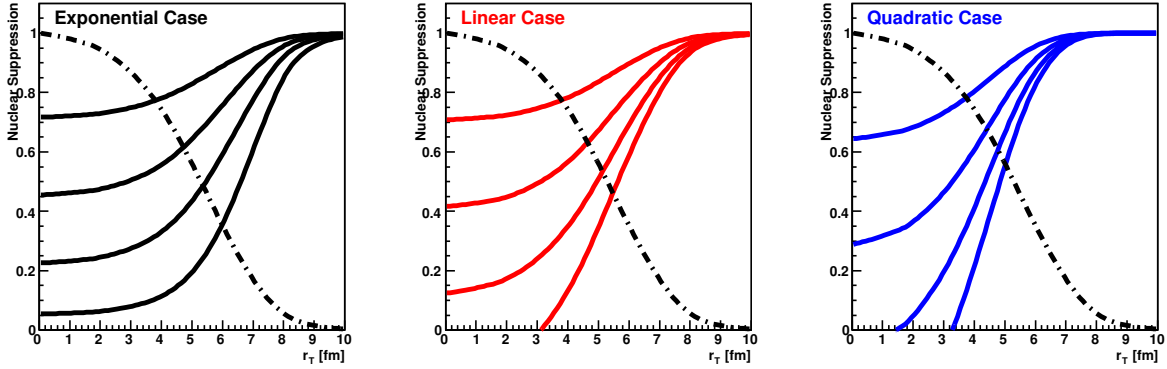


FIG. 5. Shown are the modification dependencies $M(r_T)$ for the three geometry cases (exponential, linear, and quadratic) assuming four different average $R_{dAu}(0-100\%)$ values – 0.8, 0.6, 0.4, 0.2 (corresponding to the top to bottom curves in each case). The dot-dashed black line is the shape of the N_{tube} distribution versus r_T , normalized to one at $r_T = 0$ for reference.

middle (right) panel shows the same results for the linear (quadratic) case. As a consequence of the linear and quadratic functional forms, $M(r_T)$ has negative values for small r_T when the geometry-averaged modification is less than 0.4 (0.6) for the linear (quadratic) cases. This unphysical result can be removed by forcing the modification to be positive-definite, but then one has to recalculate the corresponding a parameters. In the analysis presented in this paper, the modification values from the nPDF do not typically reach these low values and thus we have not had to recalculate the results. However careful attention to this problem will be crucial for cases with larger modifications (for example more forward rapidity J/ψ measurements or very low- x measurements at the Large Hadron Collider in $p + A$ and $A + A$).

There are two final ingredients needed to map the nPDF modifications onto the final state J/ψ suppression. These are the distribution of Bjorken x_2 and Q^2 for the parton-parton processes that contribute to the J/ψ production and the mixture of $g + g$, $g + q$, and $q + \bar{q}$ processes. The simplest relationship between the J/ψ and partonic kinematics arises under the assumption that the production is a $2 \rightarrow 1$ process, for example $g + g \rightarrow J/\psi$. Invoking conservation of energy and momentum the production of a J/ψ with $p_T = 0$ GeV/ c results in the following relationship between J/ψ rapidity (y) and parton momentum fraction (x_2).

$$x_2 = \frac{M_{J/\psi}}{\sqrt{s_{NN}}} e^{-y} \quad (5)$$

This $2 \rightarrow 1$ process is actually forbidden by angular momentum conservation, but may approximate the correct kinematics at low p_T , or in a color evaporation picture where soft gluon emission does not significantly modify the exact correlation of x_2 and y . It has been pointed out that with a more detailed understanding of the subprocesses that contribute to J/ψ production, one can utilize a more exact map of x_2 and Q^2 to the final J/ψ as a

function of rapidity and p_T [18–20]. The authors utilize the following relation between x_1 and x_2 that requires a full modeling of the cross section dependencies:

$$x_2 = \frac{x_1 \sqrt{p_T^2 + M^2} \sqrt{s_{NN}} e^{-y} - M^2}{\sqrt{s_{NN}} (\sqrt{s_{NN}} x_1 - \sqrt{p_T^2 + M^2} e^y)} \quad (6)$$

This relation is exact for a $2 \rightarrow 2$ process where one outgoing particle is an on-shell J/ψ and the other particle is massless.

Shown in Figure 6 (upper panel) is the correlation of Bjorken x_2 with the J/ψ rapidity in the $2 \rightarrow 1$ case. This is compared with a scatter-plot showing calculation results from PYTHIA 6.416 [21] with the NRQCD setting for J/ψ production. As expected, the x_2 values for a given J/ψ rapidity are shifted to larger values. Since the J/ψ $\langle p_T \rangle \approx 2.2$ GeV/ c , there must be a balancing particle(s), which requires larger available energy. Also, the emission of a balancing gluon, for example, will smear the rapidity of the J/ψ relative to the $2 \rightarrow 1$ calculation. Also shown are the $\langle x_2 \rangle$ values as a function of rapidity for the PYTHIA $g + g$ color singlet channel (black), $g + g$ color octet channel (blue), and the $q + g$ color octet channel (red). The mean x_2 value can be misleading since it may have a large influence from a small fraction of high- x events. Thus, in the lower panel we show the $\log(x_2)$ distribution for the J/ψ rapidity $2.0 < y < 2.4$ for the three different contributions. The majority of processes for this rapidity involve $x_2 \approx 0.002$, but with a more significant high- x tail in the octet cases. Note that the underlying PYTHIA production does not obey the $2 \rightarrow 2$ kinematics of Eqn. 6, since there is initial-state k_T and many of the octet production channels involve more than two final-state particles.

We now incorporate all of the following items: (1) Monte Carlo Glauber, (2) deuteron and gold nuclear geometries, (3) EPS09 nPDF parameter set, (4) geometric dependence assumption for nPDF (i.e. linear, quadratic, exponential), (5) kinematic mapping (g , q , \bar{q} , x_2 , $Q^2 \rightarrow$

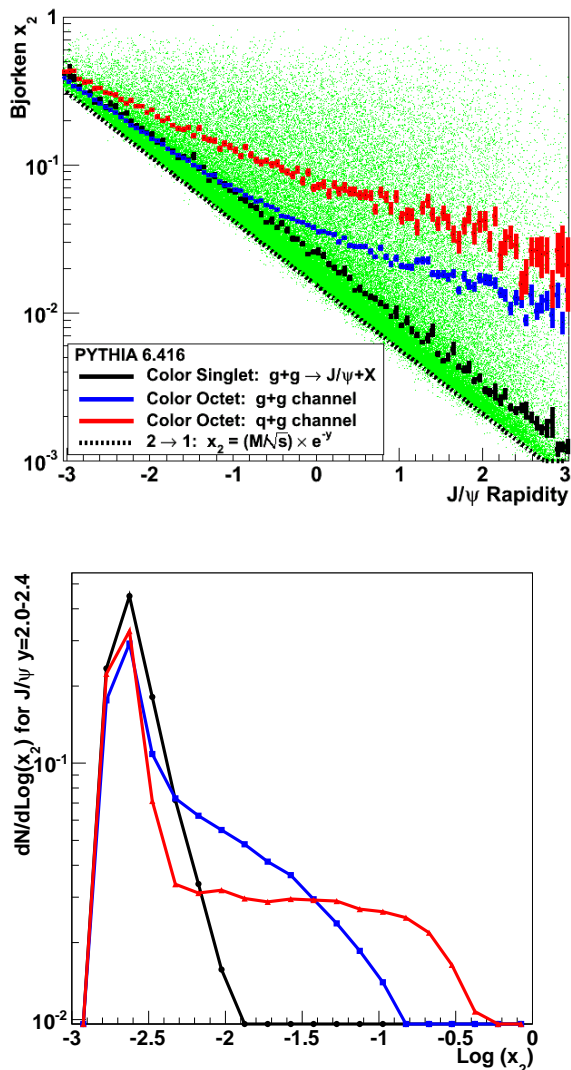


FIG. 6. (Upper panel) The kinematic correlations between the J/ψ rapidity and Bjorken x_2 for the $2 \rightarrow 1$ process compared with a scatter-plot showing calculations from PYTHIA 6.416 with the NRQCD setting for J/ψ production. The $\langle x_2 \rangle$ values are shown for three different production mechanisms within PYTHIA 6.416. (Lower panel) Shown are the x_2 distributions for J/ψ produced with rapidity $2.0 < y < 2.2$ for the three different PYTHIA production mechanisms (black for $g+g$ color singlet, blue for $g+g$ color octet, and red for $q+g$ color octet).

J/ψ y , p_T). We then add the second factorized part of the calculation for the σ_{br} by checking all nucleons on the back side of the nucleus (i.e. $z_{nucleon} > z_{binary}$) for whether the $c\bar{c}$ pair breaks up. Note that although the calculations are factorized, the results are auto-correlated by the geometry. For example, a binary collision occurring near $r_T = 0$ has a larger nPDF modification and also a larger probability for breakup. These auto-correlations are important to account for, and have been previously explored in terms of k_T kicks broadening the p_T distribution [22, 23].

Two additional benefits of this Monte Carlo Glauber approach with full fluctuations are that we can model the exact PHENIX experimental $d+Au$ centrality selection event-by-event and that we never project onto an averaged quantity (eg. the average impact parameter for each centrality class) and then calculate the modification for that average quantity.

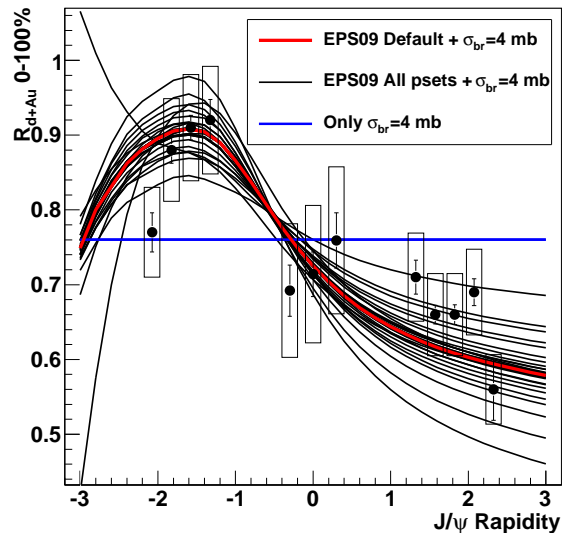


FIG. 7. Shown is the J/ψ nuclear modification factor R_{dAu} for 0-100% interaction centrality as a function of rapidity. The calculations include the EPS09 nPDFs with the linear geometric dependence and $2 \rightarrow 1$ kinematics. The yellow band shows the limits from all 31 EPS09 nPDF variations, but should not be interpreted as a one-standard deviation uncertainty band. The PHENIX experimental data are shown as black points. The lines are the point-to-point uncorrelated uncertainties and the boxes are the point-to-point correlated systematic uncertainties. Not shown is the additional $\pm 7.8\%$ global scale uncertainty.

III. CALCULATION RESULTS

Putting all these pieces together, we show an example calculation in Figure 7 of the J/ψ nuclear modification R_{dAu} as a function of rapidity for 0-100% of the $d+Au$ inelastic cross section. In this example, we utilize the $2 \rightarrow 1$ exact process mapping and the linear geometric dependence of the nPDFs. We show the default EPS09 result with a $\sigma_{br} = 4$ mb (red curve), all 30 other variations for EPS09 with a $\sigma_{br} = 4$ mb (black curves), and a calculation assuming no nPDF modification with $\sigma_{br} = 4$ mb (blue curve). The PHENIX experiment has recently reported high statistics J/ψ $d+Au$ at $\sqrt{s_{NN}} = 200$ GeV nuclear modification factors as a function of rapidity [17] which are also shown in Figure 7. Within systematic uncertainties from the experimental data and theoretical calculation, reasonable agreement is obtained.

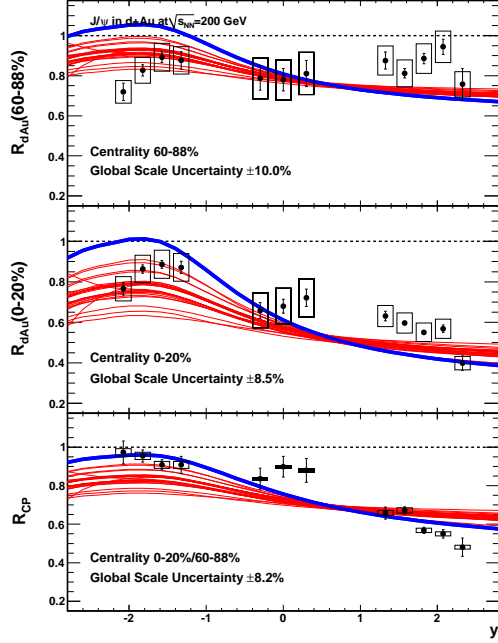


FIG. 8. Comparison of PHENIX data with calculations (red curves) using the 31 EPS09 parameter sets with linear nuclear thickness dependence. Each EPS09 parameter set is shown for its own best fit σ_{br} value. The blue curve shows the best fit for the best set, obtained with EPS09 set 17 and $\sigma_{br} = 3.2$ mb.

We emphasize that this calculation utilized the $2 \rightarrow 1$ kinematics. We have performed the same calculation using the various PYTHIA kinematics and find only a very modest decrease (smoothing out) of the rapidity dependence. The rapidity dependence in the calculation comes entirely from the nPDF dependence on x_2 and Q^2 . Thus, utilizing the PYTHIA kinematics leads to a slight blurring of this relation and a general shift to larger x_2 values, as expected from Figure 6. This flattening of the R_{dAu} versus rapidity goes in the opposite direction of the experimental data; however, the uncertainties in the nPDFs and other physics do not allow for any conclusion about the underlying production process.

Shown in Figure 8 are the PHENIX experimental results for R_{dAu} for peripheral events 60-88% (top panel), R_{dAu} for central events 0-20% (middle panel), and the ratio between them R_{CP} 0-20% / 60-88% (lower panel). Note that the significant systematic uncertainties that can modify the rapidity dependence of the modification, referred to by PHENIX as type-B systematics, largely cancel in the R_{CP} ratio.

We utilize the r_T distributions for each centrality class shown in Figure 3 of the PHENIX publication [17] to compute the expected modification in each centrality. There are many different statistical fits one can perform

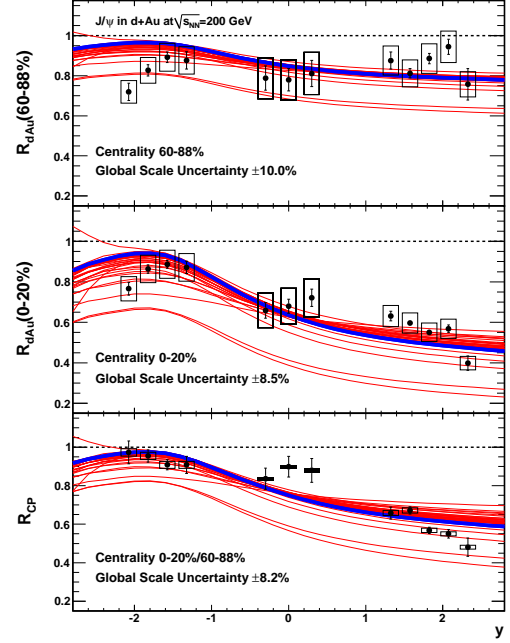


FIG. 9. Comparison of PHENIX data with calculations (red curves) using the 31 EPS09 parameter sets with quadratic nuclear thickness dependence. Each EPS09 parameter set is shown for its own best fit σ_{br} value. The blue curve shows the best fit for the best set, obtained with EPS09 set 30 and $\sigma_{br} = 3.4$ mb.

between the experimental data and our theoretical calculations. In this case, we perform a modified- χ^2 ($\tilde{\chi}^2$) fit to just the R_{CP} data (which provides by far the best constraint on the rapidity dependence). The $\tilde{\chi}^2$ fit method that accounts for both statistical and systematic uncertainties is detailed in [24].

We have chosen again to utilize the $2 \rightarrow 1$ kinematics and consider the linear, quadratic, and exponential geometric dependencies for the nPDFs. Shown in Figure 8 are the results for the linear geometric dependence. Each red curve represents one of the 31 EPS09 nPDF parameter sets and the best fit σ_{br} value for that parameter set (*ie.* minimum $\tilde{\chi}^2$) to the R_{CP} data. The calculation corresponding to that red curve is then also shown for R_{dAu} peripheral and central in the upper and middle panels, respectively. The blue curve represents the best fit overall for all combinations for EPS09 parameter sets and σ_{br} values – corresponding to EPS09 nPDF parameter set 17 and a $\sigma_{br} = 3.2$ mb. However, even this best fit has a $\tilde{\chi}^2 = 41.5$ which corresponds to an extremely poor fit (*ie.* probability less than 10^{-4}). The result with the geometric nPDF exponential case are similar with the best fit from EPS09 nPDF parameter set 17 and $\sigma_{br} = 4.2$ mb and a poor $\tilde{\chi}^2 = 50.6$.

Shown in Figure 9 are the results for the quadratic ge-

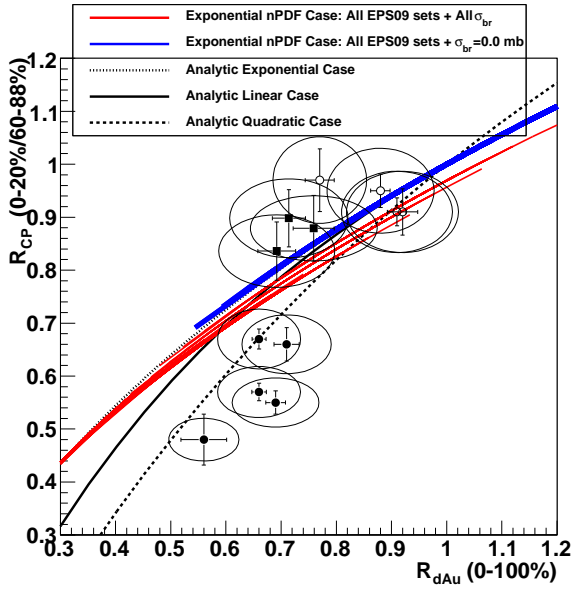


FIG. 10. The points are the PHENIX J/ψ R_{CP} versus R_{dAu} . The ellipses are the one-standard deviation contours for the systematic uncertainties. The open circles, closed squares, and closed circles are from backward, mid, and forward rapidity respectively. The black curves are analytic calculations assuming a purely exponential, linear, and quadratic geometric dependence for the nuclear modification [17]. The blue lines are the full calculation, using an exponential thickness dependence for the shadowing, for all EPS09 nPDF parameter sets with $\sigma_{br} = 0$. The red lines are the full calculation for all EPS09 nPDF parameter sets with all σ_{br} values.

ometric dependence. In this case the best fit corresponds to EPS09 parameter set 30 and $\sigma_{br} = 3.4$ mb. Again, even this best fit has a $\chi^2 = 46.3$ which corresponds to an extremely poor fit. One notable feature that may appear counter-intuitive is that for some EPS09 nPDF parameter sets, the best fit shown by the red curve appears very far below the R_{CP} data points. Because the rapidity shape is so poorly matched, it is possible that a better fit is obtained with the χ^2 under the assumption that the global scale uncertainty of 8.2% has a three standard deviation fluctuation low.

IV. NEW GEOMETRIC CONSTRAINTS

In [17], the PHENIX collaboration presented a new way of using the experimental data to test and constrain the geometric dependence of the combined nuclear effects. By plotting the R_{CP} value (0-20%/60-88%) versus the geometry-averaged nuclear modification R_{dAu} (0-100%), there are constrained parametric dependencies for the linear, exponential, and quadratic cases. In [17], the analytic parameterization for $M(r_T)$ as a function of the average $\Lambda(r_T)$ was used to compare the nuclear modification in all centralities for a given parameter a value. For a given geometric dependence, varying

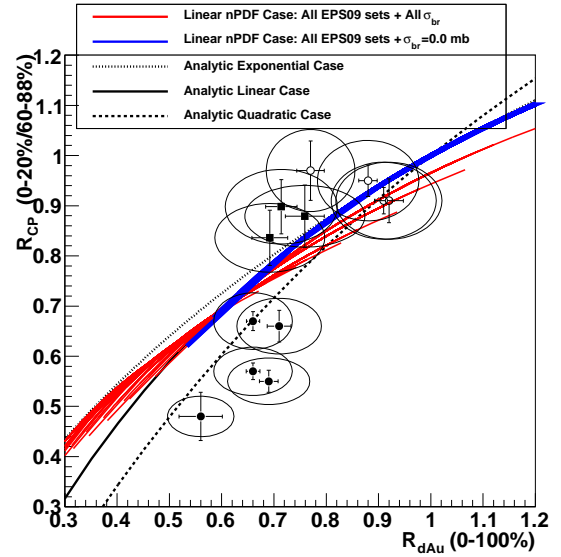


FIG. 11. The points are the PHENIX J/ψ R_{CP} versus R_{dAu} . The ellipses are the one-standard deviation contours for the systematic uncertainties. The open circles, closed squares, and closed circles are from backward, mid, and forward rapidity respectively. The black curves are analytic calculations assuming a purely exponential, linear, and quadratic geometric dependence for the nuclear modification [17]. The blue lines are the full calculation, using a linear thickness dependence for the shadowing, for all EPS09 nPDF parameter sets with $\sigma_{br} = 0$. The red lines are the full calculation for all EPS09 nPDF parameter sets with all σ_{br} values.

the values of a results in a locus of points for a constrained relationship between R_{dAu} and R_{CP} . Shown in Figure 10 as dotted, solid, and dashed black lines are the result of that analytic calculation for the exponential, linear, and quadratic cases respectively. To be clear, these curves are calculated purely from a Monte Carlo Glauber geometry, the average density-weighted nuclear thickness $\Lambda(r_T)$, and the simple geometric dependence equation (i.e. no specific model of nPDFs, σ_{br} , etc). Also shown are the PHENIX experimental data with the lines as point-to-point uncorrelated uncertainties and the ellipses as one-standard deviation contours from the combined systematic uncertainties. As stated in [17], this demonstrates that the forward rapidity J/ψ data cannot be reconciled with an exponential or linear geometric dependence for the nuclear modification.

We test this picture further by additionally plotting the results from our calculations using the EPS09 nPDFs and σ_{br} model. In Figure 10, we show all EPS09 nPDF parameter sets using the exponential geometric dependence, a range of values of σ_{br} (from 0-18 mb in 2 mb steps) and the full range of rapidity values (as red lines). The subset corresponding to $\sigma_{br} = 0$ are shown as blue lines. As expected, since the nPDF dependence is exponential, the blue lines fall almost perfectly on the analytic pure exponential case (dotted black line). With the additional σ_{br} contribution which also has an exponential geometric

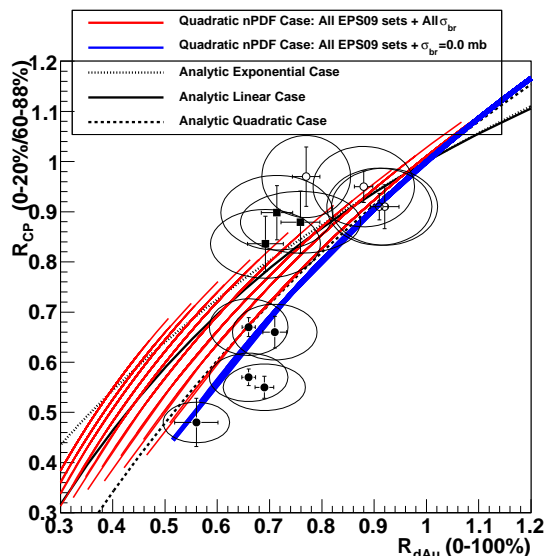


FIG. 12. The points are the PHENIX J/ψ R_{CP} versus R_{dAu} . The ellipses are the one-standard deviation contours for the systematic uncertainties. The open circles, closed squares, and closed circles are from backward, mid, and forward rapidity respectively. The black curves are analytic calculations assuming a purely exponential, linear, and quadratic geometric dependence for the nuclear modification [17]. The blue lines are the full calculation, using a quadratic thickness dependence for the shadowing, for all EPS09 nPDF parameter sets with $\sigma_{br} = 0$. The red lines are the full calculation for all EPS09 nPDF parameter sets with all σ_{br} values.

dependence, we expected that everything would collapse onto the same line. However, with two competing effects $R_{dAu}(0-100\%) = 1$ does not always equate with the trivial case of no modification, but can also occur if the two effects average to 1. In the latter case, R_{CP} need not be 1. Specifically in our case, in the backward rapidity region the nPDF leads to an enhancement (anti-shadowing) and the σ_{br} to a suppression. This competition can lead to the case where $R_{dAu}(0-100\%) = 1$, while the $R_{CP} \neq 1$ (*ie.* some slight enhancement in peripheral events due to the nPDF effect and some slight suppression in central events due to the σ_{br} effect). This effect leads to the slight splitting of the lines for values near $R_{dAu} = 1$.

Shown in Figure 11 are the same quantities for the nPDF linear case in our calculation. Again, the case with $\sigma_{br} = 0$ leaves only the purely linear nPDF and thus the blue lines collapse onto the analytic linear case (solid black curve). The red curves for all $\sigma_{br} > 0$ cases result in a geometric dependence that is part linear and part exponential. Thus, one sees that for larger suppressions (also larger σ_{br} values), the red curves move between the analytic linear case to the analytic exponential case. One again sees some cases of $R_{dAu}(0-100\%) = 1$, while the R_{CP} is not equal to one for the same reason as described above.

Lastly, in Figure 12, we show the quadratic case. In this case with $\sigma_{br} = 0$ the blue lines are close to the black

dashed analytic quadratic case, but not perfectly. This is due to the inclusion of fluctuations in the thickness included in our full calculation shown here. As one increases the value of σ_{br} in 2 mb increments one sees the red lines moving to the left as the exponential geometric dependence from σ_{br} dominates over the quadratic nPDF effect.

This full suite of curves reveals that even attempting to fit just the forward rapidity data with a larger and larger σ_{br} will not successfully capture the full centrality dependence (even using the quadratic nPDF contribution).

The results of fitting R_{CP} versus rapidity shown in Figures 8 and 9 demonstrated that no variation in the model (e.g. EPS09 nPDF parameter sets, nPDF geometric dependence, single σ_{br} values, etc.) can be reconciled with the full rapidity and centrality dependence of the experimental data. It is possible that σ_{br} may have a rapidity dependence due to the different relative velocity of the $c\bar{c}$ pair with respect to the target nucleons. A naïve expectation is that a shorter time spent in the nucleus should result in a smaller σ_{br} due to a smaller growth in the physical size of the $c\bar{c}$ pair towards that of the final state J/ψ . However, in order to attempt to reconcile the data with a rapidity-dependent σ_{br} the cross section would need to be much larger at larger rapidity (as shown in [25] in Section 5.2). In fact, the results from the R_{CP} and R_{dAu} correlation indicate that no value of σ_{br} (even with an independent value for forward rapidity) can properly describe the centrality dependence. This fact can be understood by noting that no matter how large a value of σ_{br} one uses, the geometric dependence is always exponential.

Another possibility is that the geometric dependence of the nPDF varies with rapidity. While this is possible, without direct theoretical guidance or other experimental constraints, one would just be arbitrarily fitting the data. In the next section we consider two additional models in the literature that have different physics than this framework.

V. ADDITIONAL MODEL COMPARISONS

One proposal for physics beyond the factorized nPDF and σ_{br} involves calculations incorporating gluon saturation (non-linear evolution of the gluon distributions at low x). In the PHENIX paper [17], the data were compared with a color glass condensate calculation [28] that incorporated suppression at low x from gluon saturation and enhancement from double-gluon exchange diagrams. More recent calculations following this framework [26] include a more accurate treatment of the nuclear geometry and the dipole-nucleus scattering amplitudes, and are consistent with recent calculations for the Au+Au case [29]. Shown in Figure 13 (left panel) is the calculated J/ψ nuclear modification for different rapidities as a function of the d +Au event impact parameter (b). It is

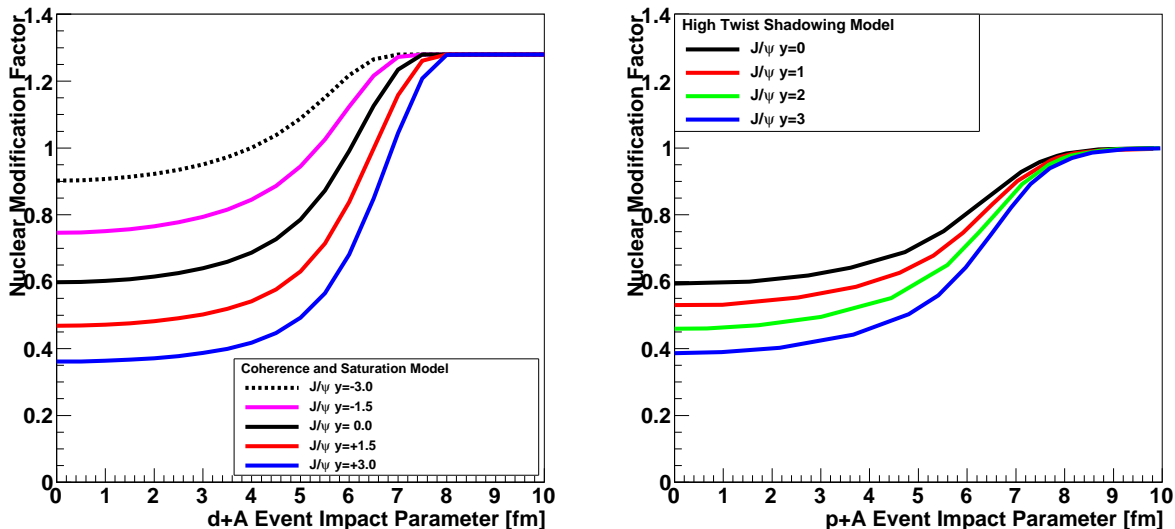


FIG. 13. (Left Panel) Shown are J/ψ nuclear modification results from the color glass condensate calculation including gluon saturation from [26] as a function of event impact parameter in $d+Au$ reactions. (Right Panel) Shown are the results of a coherence and color transparency calculation [27] for the J/ψ nuclear modification as a function of event impact parameter in $p+Au$ reactions.

notable that for large b there is a 30% nuclear enhancement, even though the coherence is only an effect in the longitudinal direction and the local nuclear density for these large- b events is small.

In an alternative calculation presented in [27], the J/ψ production is controlled by coherence and color transparency effects. Shown in Figure 13 (right panel) is the calculated J/ψ nuclear modification factor as a function of event impact parameter in $p+Au$ reactions.

In either case, we can fold these dependencies with the $d+Au$ event impact parameter distributions or the r_T distribution (for the $p+Au$ predictions), and compute the R_{dAu} and R_{CP} modification factors to compare with the PHENIX experimental data. These comparisons are shown in Figure 14. We also show for comparison the EPS09 nPDF default with linear geometric dependence and $\sigma_{br} = 4$ mb. The calculation from [27] yields similar results to the EPS09 nPDF and σ_{br} calculation, and has insufficient suppression at the most forward rapidity. The color glass condensate calculation shows better agreement at forward rapidity, though the rapidity dependence is not as steep as that of the R_{CP} experimental data. But it has substantial disagreement with the data at mid and backward rapidities. Note that that calculation assumes coherence over the entire longitudinal extent of the nucleus, but this coherence approximation is no longer valid at some higher- x values (*ie.* moving towards mid and then backward rapidity). It is also no longer valid for low densities that occur at large impact parameter values. Thus, the result that for large impact parameters the color glass condensate calculation approaches $R_{dAu} \approx 1.3$ (shown in the left panel of Fig-

ure 13) is likely to simply be outside the range of validity of the calculation.

VI. INITIAL-STATE ENERGY LOSS

Another physical effect that has been proposed is that of initial state parton energy loss. The very forward rapidity J/ψ are produced from a high x_1 parton (from the deuteron) and a low x_2 parton (from the gold nucleus). If the high x_1 parton from the deuteron loses some energy before the hard scattering, this will result in a lower J/ψ production probability and a shift backward in rapidity for any produced particles (including the J/ψ). This framework has been used in an attempt to reconcile lower energy Drell-Yan data in $p+A$ collisions (see for example [30, 31]). However, the same data have also been interpreted in terms of nuclear shadowing models instead of large initial-state energy loss. It is unclear if these experimental data sets can be reconciled with the same energy loss, and whether that provides a consistent picture for all such $p(d)+A$ data.

More recently, in [32] a calculation is presented of initial-state parton energy loss and its impact on Drell-Yan production with predictions for measurements in $p+A$ collisions. In the case of initial-state radiative energy loss, they predict that $\Delta E/E \propto L$, where L is the path through the nucleus prior to the hard scattering. Data from experiment E906 at Fermilab will directly address this prediction, and in the clean Drell-Yan channel without final state effects [33].

As a preliminary investigation of the impact of initial-

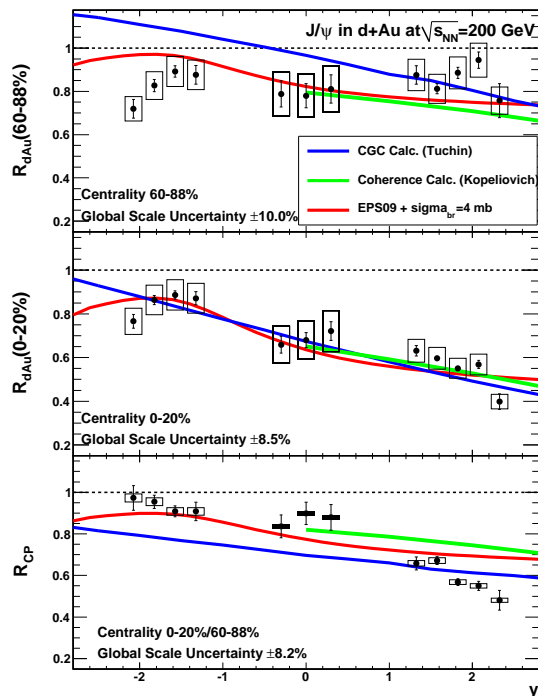


FIG. 14. Shown are the PHENIX experimental data for J/ψ R_{dAu} peripheral (top) R_{dAu} central (middle), and R_{CP} 0-20%/60-88% (bottom) as a function of rapidity. The green curve results from [27] with coherence effects and color transparency. The blue curve is the color glass condensate calculation [26]. The red curve is our calculation with nPDF EPS09 default set=1 with a linear geometric dependence and $\sigma_{br} = 4$ mb.

state parton energy loss, we have implemented this mechanism in our calculation (in addition to the nPDF and σ_{br} contributions). Within the Monte Carlo Glauber, we also calculate $N_{tube}[before]$, the number of Au nucleus nucleons in the tube that have a z location prior to the z position of the binary collision of interest. We posit that the initial-state energy loss is proportional to $N_{tube}[before]$, which is the same as being proportional to the path L , with the inclusion of local fluctuations. For this calculation, we have utilized the PYTHIA production $g + g \rightarrow J/\psi + X$ kinematics. For each binary collision location, we randomly select a PYTHIA x_1, x_2 combination and the average J/ψ rapidity for those kinematics. We then calculate the expected x_1 shift due to the energy loss corresponding to the particular $N_{tube}[before]$ value. From this information, we calculate the decrease in the probability for these partons to produce a $c\bar{c}$ pair and the new (lower) average final state J/ψ rapidity with the modified parton kinematics. We have varied the proportionality constant for the initial-state energy loss in the $N_{tube}[before]$ dependence.

In Figure 15 (left panel), we show the calculation results including only initial state parton energy loss (i.e. no nPDF modification and $\sigma_{br} = 0$). One observes a

larger suppression at forward rapidity, and in fact a modest enhancement at backward rapidity. In Figure 15 (right panel), we show the results when now assuming a quadratic path dependence for the energy loss (i.e. $\Delta E/E \propto L^2$). In this case, for large coefficients in the proportionality constant, there is large suppression at all rapidities. For either the L or L^2 dependence, one cannot achieve good agreement with the experimental data with initial-state parton energy loss alone.

We then include all three nuclear effects (nPDF modification, σ_{br} , and initial-state parton energy loss), and vary the EPS09 nPDF parameter set and fit for the best σ_{br} and energy loss coefficient. In Figure 16 (left panel), we have found the best χ^2 from the fit to the R_{CP} . The blue curve represents the best overall fit for all EPS09 parameterizations and the optimal σ_{br} and initial-state energy loss coefficient. The best fit gives a reasonable description of the R_{CP} and corresponds to EPS09 parameter set 23, $\sigma_{br} = 3$ mb, and $\Delta E/E \approx 0.05/\text{fm} \times L$ (converting the average $N_{tube}[before]$ to a length through normal nuclear matter density). The $\chi^2 = 20.2$ which is a better fit than without the initial-state energy loss, but still gives a probability of less than 5%. However, more striking is that with a reasonable fit to the R_{CP} , there is no global agreement with the overall suppression for R_{dAu} in peripheral or central events.

In Figure 16 (right panel), we show the same quantities, but now assuming that the initial-state energy loss is quadratic in the path or $N_{tube}[before]$. In this case the best fit to R_{CP} has EPS09 parameter set 5, $\sigma_{br} = 4$ mb, and the initial-state energy loss corresponds to approximately $\Delta E/E \approx 0.005/\text{fm}^2 \times L^2$. Again there is no overall global good fit for R_{dAu} and R_{CP} .

These results are a first look in comparing the simplest initial-state energy loss calculation to these J/ψ data. We have not included Poisson fluctuations of the radiated quanta, which are important when one is near the very high- x_1 limit as pointed out in [32]. However, in their calculation they have not included the important fluctuations in the L value itself, as we have done through utilizing $N_{tube}[before]$. It is premature to draw any firm conclusions about the implications for initial-state parton energy loss from these comparisons with J/ψ data alone. Further calculations are necessary, as well as comparisons to observables from other collision energies and other final state produced particles.

VII. SUMMARY

In this paper, we have presented an extension of calculations for J/ψ nuclear modifications including modified parton distribution functions (nPDFs) and fit parameter σ_{br} . Utilizing the full set of EPS09 nPDFs and three different postulated geometric dependencies, we find that the calculations cannot be reconciled with the full rapidity and centrality dependence of the PHENIX $d+Au$ J/ψ data for any nPDF variation and any σ_{br} value. Ad-

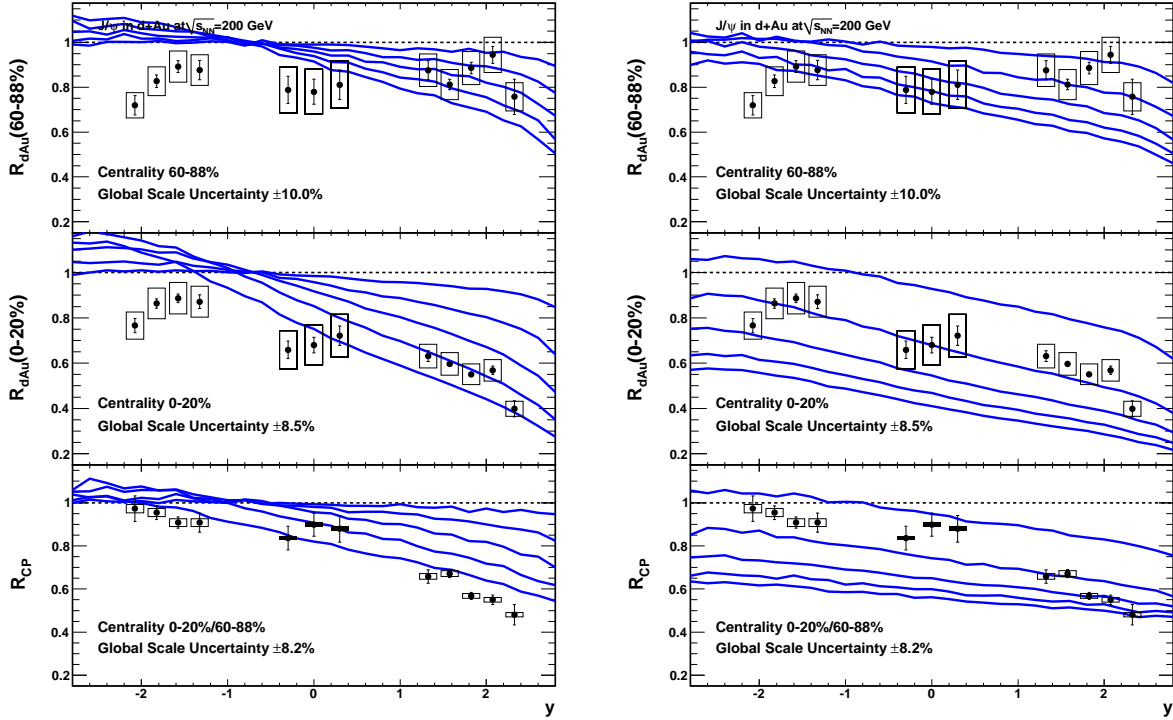


FIG. 15. (Left Panel) Calculation including initial-state parton energy loss only and with $\Delta E/E \propto L$ or equivalently in our case with fluctuations to $N_{tube}[before]$. The curves correspond to coefficients of 0.01/fm, 0.03/fm, 0.05/fm, 0.07/fm, and 0.09/fm (from upper to lower in order). (Right Panel) Calculation including initial-state parton energy loss only and with $\Delta E/E \propto L^2$ or equivalently in our case with fluctuations to $N_{tube}[before]^2$. The curves correspond to coefficients of 0.005/fm², 0.015/fm², 0.025/fm², 0.035/fm², and 0.045/fm² (from upper to lower in order).

ditionally, the comparison with R_{CP} versus R_{dAu} indicates that even a much larger σ_{br} at forward rapidity cannot reconcile the calculation with the data, since the σ_{br} contribution always has an exponential geometric dependence. We also compare to two different coherence calculations and find no agreement across all rapidities and centralities. Most likely new physics beyond these calculations is a significant contributor, perhaps initial-state parton energy loss. A first look at a simple parameterization of initial-state energy loss allows a better description of the J/ψ R_{CP} , but without a good simultaneous description of R_{dAu} . Additional constraints from Drell-Yan and direct photon observables at forward rapidity and at different $\sqrt{s_{NN}}$ energies may be necessary to disentangle these effects.

ACKNOWLEDGMENTS

We thank Kirill Tuchin for providing us with the color glass condensate calculation results and useful discussions, and Michael Stone for generating the PYTHIA event samples. We also acknowledge useful discussions with Mike Leitch, Darren McGlinchy, and Ramona Vogt. JLN and MGW acknowledge funding from the Division of Nuclear Physics of the U.S. Department of Energy under Grant No. DE-FG02-00ER41152. LALL acknowledges that this work was performed under the auspices of the U.S. Department of Energy by Lawrence Livermore National Laboratory under Contract DE-AC52-07NA27344. ADF acknowledges funding from the National Science Foundation under contract PHY-07-56474. We also thank the Institute for Nuclear Theory at the University of Washington for its hospitality and the Department of Energy for partial support during some of this work.

[1] C. Lourenco, R. Vogt, and H. K. Woehri, JHEP **0902**, 014 (2009), arXiv:0901.3054.

[2] A. Adare *et al.* (PHENIX Collaboration), Phys.Rev. **C77**, 024912 (2008), arXiv:0711.3917.

[3] R. Vogt, Phys. Rev. **C71**, 054902 (2005).

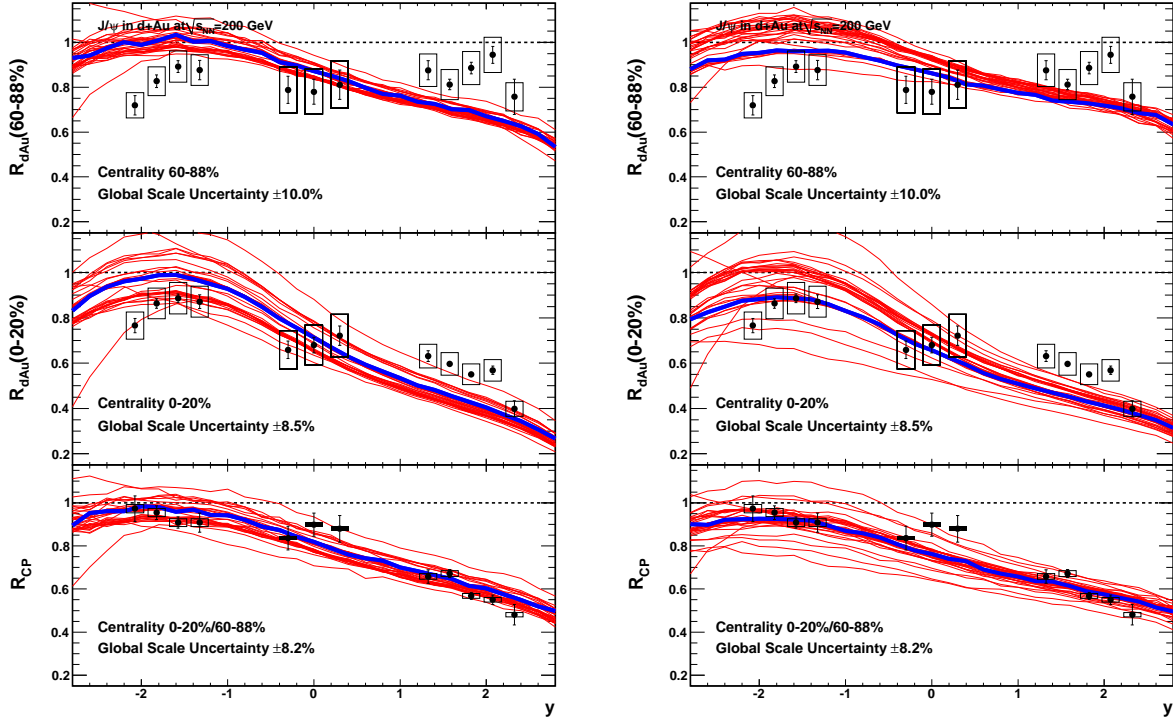


FIG. 16. (Left Panel) Best fit including initial-state parton energy loss assuming the loss is proportional to $N_{tube}[before]$. (Right Panel) Best fit including initial-state parton energy loss assuming the loss is proportional to $N_{tube}[before]^2$.

- [4] D. Kharzeev, C. Lourenco, M. Nardi, and H. Satz, Z.Phys. **C74**, 307 (1997), hep-ph/9612217.
- [5] K. J. Eskola, H. Paukkunen, and C. A. Salgado, JHEP **04**, 065 (2009).
- [6] S. J. Brodsky and J.-P. Lansberg (2009).
- [7] J. P. Lansberg, Eur. Phys. J. **C61**, 693 (2009).
- [8] C. Lourenco, P. Faccioli, and H. K. Wohri, Lect. Notes Phys. **785**, 199 (2010).
- [9] M. L. Miller, K. Reygers, S. J. Sanders, and P. Steinberg, Ann. Rev. Nucl. Part. Sci. **57**, 205 (2007).
- [10] S. Klein and R. Vogt, Phys.Rev.Lett. **91**, 142301 (2003), nucl-th/0305046.
- [11] B. Alver and G. Roland, Phys.Rev. **C81**, 054905 (2010), arXiv:1003.0194.
- [12] P. Sorensen, J.Phys.G **G37**, 094011 (2010), arXiv:1002.4878.
- [13] J. Nagle, P. Steinberg, and W. Zajc, Phys.Rev. **C81**, 024901 (2010), arXiv:0908.3684.
- [14] H.-J. Drescher, A. Dumitru, C. Gombeaud, and J.-Y. Ollitrault, Phys.Rev. **C76**, 024905 (2007), arXiv:0704.3553.
- [15] B. Alver *et al.* (PHOBOS Collaboration), Phys.Rev.Lett. **98**, 242302 (2007), nucl-ex/0610037.
- [16] K. Nakamura *et al.* (Particle Data Group), J. Phys. **G37**, 075021 (2010).
- [17] A. Adare, S. Afanasiev, C. Aidala, N. Ajitanand, Y. Akiba, *et al.* (2010), arXiv:1010.1246.
- [18] A. Rakotozafindrabe, E. Ferreiro, F. Fleuret, and J. Lansberg, J.Phys.G **G37**, 094055 (2010), arXiv:1002.2351.
- [19] E. Ferreiro, F. Fleuret, J. Lansberg, and A. Rakotozafindrabe, Phys.Rev. **C81**, 064911 (2010), arXiv:0912.4498.
- [20] E. Ferreiro, F. Fleuret, J. Lansberg, and A. Rakotozafindrabe, Phys.Lett. **B680**, 50 (2009), arXiv:0809.4684.
- [21] T. Sjostrand, S. Mrenna, and P. Skands, JHEP **05**, 026 (2006).
- [22] J. Nagle and M. Bennett, Phys.Lett. **B465**, 21 (1999), nucl-th/9907004.
- [23] D. Kharzeev, M. Nardi, and H. Satz, Phys.Lett. **B405**, 14 (1997), hep-ph/9702273.
- [24] A. Adare *et al.* (PHENIX Collaboration), Phys.Rev. **C77**, 064907 (2008), arXiv:0801.1665.
- [25] N. Brambilla, S. Eidelman, B. Heltsley, R. Vogt, G. Bodwin, *et al.* (2010), arXiv:1010.5827.
- [26] K. Tuchin (private communication).
- [27] B. Kopeliovich, I. Potashnikova, H. Pirner, and I. Schmidt (2010), arXiv:1008.4272.
- [28] D. Kharzeev and K. Tuchin, Nucl. Phys. **A770**, 40 (2006).
- [29] K. Tuchin, Nucl. Phys. **A830**, 243c (2009).
- [30] J. Moss, G. Garvey, M. Johnson, M. Leitch, P. McGaughey, *et al.* pp. 576–580 (2001), hep-ex/0109014.
- [31] M. B. Johnson *et al.*, Phys. Rev. **C65**, 025203 (2002).
- [32] R. Neufeld, I. Vitev, and B. Zhang (2010), 1010.3708.
- [33] P. E. Reimer, J.Phys.G **G34**, S107 (2007), 0704.3621.